ARTICLE

Side chain: backbone projections in aromatic and ASX residues from NMR cross-correlated relaxation

Beat Vögeli · Roland Riek

Abstract The measurements of cross-correlated relaxation rates between H^N–N and C^β–C^γ intraresidual and sequential dipolar interactions is demonstrated in ASN, ASP and aromatic residues. The experiment can be used for deuterated samples and no additional knowledge such as Karplus parametrizations is required for the analysis. The data constitutes a new type of information since no other method relates the C^β–C^γ bond to H^N–N. Using this method the dominant populations of rotamer states of $\chi 1$ can be readily cross checked provided that φ or ψ are known. In addition, dynamics on all timescales can be probed. As opposed to standard dynamics analysis of isolated bonds, the presented observables depend on relative dynamics with an interesting prospect to analyze correlated fluctuations of the two torsion angles φ or ψ with $\chi 1$. Experimental rates are compared to single conformer and ensemble representations of GB3 and ubiquitin. In particular, it is found that the recently published ubiquitin ensemble 2k39 improves the agreement obtained for 1UBQ. In general, however, input data restricting ASX and aromatic side chains in structure calculation is sparse highlighting the need for new NMR observables.

Keywords Backbone motion · Side-chain motion · Cross-correlated relaxation · GB3 · Ubiquitin · Correlated motion · $\chi 1$ Angle · Side chain

B. Vögeli (✉) · R. Riek
Laboratory of Physical Chemistry, Swiss Federal Institute of Technology, ETH-Hönggerberg, 8093 Zurich, Switzerland
e-mail: beat.voegeli@phys.chem.ethz.ch

R. Riek
The Salk Institute, 10010 N. Torrey Pines Road, La Jolla, CA 92037, USA

Introduction

A vast amount of NMR probes for the detailed structural and dynamical characterization of the backbone and the methyl groups of a protein has been proposed. These include T1 and T2 relaxation and $^{15}N\{^1H\}$-NOE (Lipari and Szabo 1982; Kay et al. 1989), relaxation dispersion experiments (Muhandin et al. 1995; Mittermaier et al. 1999; Mittermaier and Kay 2006), residual dipolar couplings (RDCs; Tjandra and Bax 1997; Meiler et al. 2001; Peti et al. 2002; Tolman 2002; Yao et al. 2008a, b; Lakomek et al. 2008; Lange et al. 2008; Salmon et al. 2009), cross-correlated relaxation (Goldman 1984; Reif et al. 1997), scalar couplings (Wüthrich 1986; Chou et al. 2003; Cavanagh et al. 2007; Vögeli et al. 2007; Markwick et al. 2009), or ^1H–^1H-NOEs (Wüthrich 1986; Brüschweiler et al. 1992; Cavanagh et al. 2007; Vögeli et al. 2009). In contrast, fewer probes are established for the characterization of local dynamics of methylene groups and these are not routinely used. Among these are ^{13}C–^{13}C NOE (Houben and Boelens 2004), ^{13}C (Nirmala and Wagner 1989; LeMaster and Kushlan 1996) and ^2H auto-relaxation (Yang et al. 1998) or $^{13}CH_2$ cross-correlated relaxation measurements (Yang et al. 1998; Zheng and Yang 2004). Probes that connect the side chain with the backbone are rare. These include NOEs between $^1H^\beta$ and $^1H^N$ or $^1H^\alpha$ as well as a suite of three-bond scalar couplings such as $J_{H\alpha H\beta}$ which can be used to define the rotamer states (Wüthrich 1986; Cavanagh et al. 2007; Schmidt 2007). For deuterated samples the proposed techniques are the measurement of the three-bond scalar couplings such as $J_{NC\gamma}$ and $J_{COC\gamma}$ (Hu and Bax 1996; Hu et al. 1997) and of ^{13}C–^{13}C RDCs (Vögeli et al. 2004). However, extraction of detailed dynamics from scalar couplings is hampered by the need of exact Karplus parametrizations which are amino-acid type

specific and difficult to obtain (Perez et al. 2001; Vögeli et al. 2007). ^{13}C–^{13}C RDCs are relatively small and the required homonuclear ^{13}C decoupling is a challenge. In contrast, cross-correlated relaxation (CCR) is a quantitative parametrization-free NMR probe that may enable a detailed structural and dynamical characterization of the side chain (Reif et al. 1997; Brutscher et al. 1998). Indeed, measurement of CCR rates between one and three spin order in three-spin systems has been proposed. Such CCR rates were initially observed for α and β hydrogens in the laboratory (Dalvit and Bodenhausen 1988) and rotating frame (Brüschweiler et al. 1989) and later for all CH_2 spin systems (Ernst and Ernst 1994). More conveniently, transverse CCR rates in four-spin systems can be used to obtain information on one or more dihedral angles between two bond vectors (Reif et al. 1997; Yang and Kay 1998; Pelupessy et al. 1999; Chiarparin et al. 1999). CCR rates between H^α–C^α and H^β–C^β dipolar interactions are able to give both structural and dynamical insights, but this method is limited to protonated proteins, demands a tedious evaluation procedure and fails for many residues (Carlomagno et al. 2003).

A special note deserves the fact that characterization of asparagine, aspartic acid and aromatic side chains lacks largely behind others. The prevailing method of choice for side-chain rotamer and dynamics studies is the ^2H relaxation study (Muhandrin et al. 1995; Hu et al. 2005; Xu et al. 2009). Recently methyl group orientation and dynamics has also been assessed by a large set of RDCs in ubiquitin thereby extending the time window to microseconds (Farès et al. 2009). The reason for this asymmetry in the method pool lies in the technical difficulty in measurements rather than in a lack of biological relevance.

Here, intraresidual and sequential CCR measurements between H^N–N and C^β–C^γ dipolar couplings in Asp, Asn and the aromatic amino acid residues are proposed. The obtained vectorial projection depends on the two torsion angles, $\chi 1$ and either φ or ψ, respectively, as well as their fluctuations. The pulse sequences are extensions of those proposed to characterize backbone motion between H^N–N and H^α–C^α (Vögeli and Yao 2009). The CCR rates are extracted from [$^{13}C^\beta$, ^{15}N] multiple quantum coherences split into quadruplets by scalar coupling to H^N and C^γ. All quadruplet components of the zero and double quantum (ZQ and DQ) [$^{13}C^\beta$, ^{15}N] coherences are evolved without intermixing and under minimal manipulation of the density operator. Thereby a minimal systematic error is guaranteed (Vögeli and Yao 2009). These CCR rates in combination with highly accurate backbone CCR rates and RDCs, and possibly side-chain RDCs, may lead to a detailed structural and dynamic picture linking the backbone and the side chain of a protein including correlated motion.

Materials and methods

Figure 1 depicts the 3D pulse sequence ct-HN(CA)CB for the measurements of intraresidual CCR rates between H^N–N and C^β–C^γ dipolar couplings in Asp, Asn and the aromatic amino acid residues which is an extension of the 3D ct-HNCA presented in reference (Vögeli and Yao 2009). $^1H^N(i)$ polarization is excited and converted into multiple quantum coherences MQ[$^{13}C^\beta(i)$, $^{15}N(i)$] via $^{15}N(i)$ in three INEPT steps. The MQ coherences are chemical-shift labeled under scalar coupling to $^1H^N(i)$ and $^{13}C^\gamma(i)$ during τ_{MQ} yielding four components (doublets of doublets) for both the ZQ and DQ coherences. Subsequently, the magnetization is converted by two transfer steps into single-quantum $^{15}N(i)$ for chemical shift labeling and transferred back to $^1H^N(i)$ for direct detection. In glycines pathways creating [$^{13}C^\alpha$, ^{15}N] MQ coherences leading to CCR rates between H^N–N and C^α–CO are also active. A ZQ and a DQ subspectrum are generated by adding and subtracting the two separately stored data sets A and B (see caption to Fig. 1 for phase cycling). Resonance assignment is straight-forward via the [^{15}N, $^1H^N$] planes (t_1, t_3). Since no pulse is applied to the relevant coupled spins (H^N and C^γ or CO) during τ_{MQ} all imperfections lead only to a decrease in signal and thereby increase the random error of the rates. It has been demonstrated that using this ACE approach systematic errors are eliminated and the overall amplitudes are very reliable (Vögeli and Yao 2009). A minor disadvantage of this method is that CO couples to N resulting in a 15 Hz splitting. This splitting is not resolved and no peak asymmetry due to ^{15}N–^{13}CO dipole/^{15}N CSA cross-correlated relaxation is observed. Note that this pulse sequence also yields [$^{13}C^\beta(i - 1)$,$^{15}N(i)$] MQ coherences relating the H^N–N to the C^β–C^γ vector of the preceding residue. However, the delays cannot be chosen such that maximal transfer is achieved for intra- and interresidual pathways simultaneously and in some cases overlap is expected.

Sequential CCR rates between H^N–N and C^β–C^γ dipolar couplings of the preceding residue are more conveniently measured with the pulse sequence ct-HN(COCA)CB which is an extension of the ct-HN(CO)CA presented in reference (Vögeli and Yao 2009; Fig. 2). The principle is the same as described above. However, magnetization from ^{15}N is transferred to $^{13}C^\alpha$ of the previous residue via ^{13}CO resulting in an additional INEPT step in the out and back transfer.

It is crucial to resolve the MQ dimension sufficiently, that is, the bottom peak width must be smaller than the peak separation. Upon insufficient resolution overlap is most likely obtained for the two most upfield and most downfield quadruplet components. Since the ratio of these is used small overlap would partially cancel.
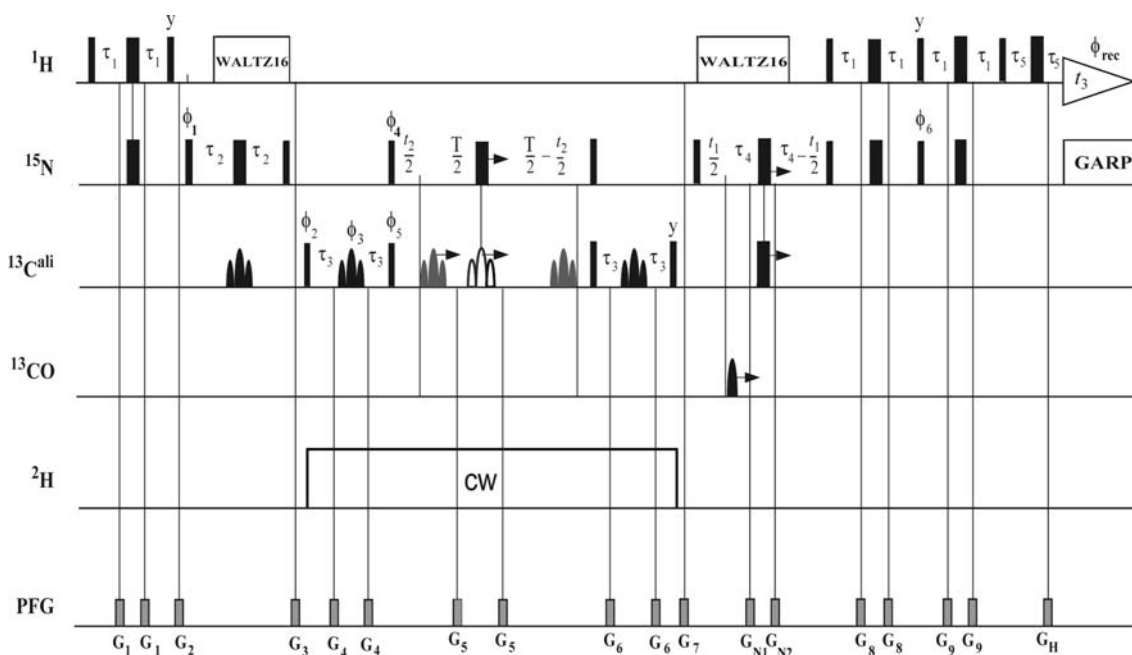
Fig. 1 Pulse sequence of the 3D ct-HN(CA)CB experiment for measurements of $R = R_{HN/C\beta C\gamma} + R_{HC\beta/NC\gamma}$ in [ASP, ASN, HIS, PHE, TYR, TRP] residues. The radio-frequency pulses on ^{1}H, ^{15}N, ^{13}C^{ali} and ^{13}C′ are applied at 4.7, 118, 44 and 174 ppm, respectively. *Narrow* and *wide bars* indicate non-selective 90° and 180° pulses. The *single curved pulse* represents a ^{13}C′-selective 180° sinc pulse of length $p_C^\pi = 150$ μs, and the *black*, *grey* and *white triple curved* ^{13}C ReBURP pulses (Geen and Freeman 1991) are C$^{\alpha/\beta}$, C$^\alpha$, or C$^\beta$-selective with $p_{C\alpha,\beta}^\pi = 500$ μs at 44 ppm, $p_{C\alpha}^\pi = 1,500$ μs at 58 ppm and $p_{C\beta}^\pi = 1,000$ μs at 28 ppm, respectively. *Vertical lines* connect centered pulses. ^{1}H-decoupling is achieved with WALTZ16 (Shaka et al. 1983) at a field strength γB_1 of 2.1 kHz and ^{15}N-decoupling is achieved with GARP (Shaka et al. 1985) at a field strength γB_1 of 1.25 kHz. The delays have the following values: $\tau_1 = 2.7$ ms, $\tau_2 = 16$ ms, $\tau_3 = 1/(4J_{C\alpha C\beta}) = 7.1$ ms, $\tau_4 = 17$ ms, $\tau_5 = 60$ μs, $\Delta = 1/(2J_{HN}) = 5.4$ ms, and $T = \tau_{MQ}-4(p_{Cali}^{\pi/2})/\pi$, where $p_{Cali}^{\pi/2}$ is the length of the rectangular ^{13}C^{ali} 90° pulse. The effective evolution during $p_{C\beta}^\pi$ is ≈ 100 μs and therefore is assumed to be of the same

length as p_N^π. Unless indicated otherwise, all radio-frequency pulses are applied with phase x. The phase cycle for the (ZQ–DQ) subspectrum is: $\phi_1 = \{x, -x\}$; $\phi_2 = \{y, y, -y, -y\}$; $\phi_3 = \{x, x, x, x, -x, -x, -x, -x\}$; $\phi_4 = \{x, x, x, x, x, x, x, x, -x, -x, -x, -x, -x, -x, -x, -x\}$; $\phi_5 = \{x, x, x, x, -x, -x, -x, -x\}$; $\phi_6 = -y$; $\phi_{rec} = \{x, -x, -x, x, x, -x, -x, x, -x, x, x, -x, -x, x, x, -x\}$. For the (ZQ + DQ) subspectrum ϕ_3, ϕ_4 and ϕ_5 are increased by 90°. Pulsed field gradients indicated on the *line marked PFG* are applied along the z-axis with duration/strength of: G_1, 1,200 μs/−9 G/cm; G_2, 2,000 μs/12 G/cm; G_3, 2,000 μs/12 G/cm; G_4, 300 μs/15 G/cm; G_5, 100 μs/18 G/cm; G_6, 300 μs/15 G/cm; G_7, 2,000 μs/12 G/cm; G_{N1}, 200 μs/18 G/cm; G_{N2}, 200 μs/−18 G/cm; G_8, 1,200 μs/10.8 G/cm; G_9, 1,200 μs/18 G/cm; G_H, 40 μs/−18 G/cm. Quadrature detection in the ^{15}N(t_1) is achieved by the ECHO-ANTIECHO method (Kay et al. 1992) applied to ϕ_6 and gradients G_{N1} and G_{N2}, and in the MQ[^{13}C$^\beta$,^{15}N](t_2) dimension by the States-TPPI method (Marion et al. 1989) applied to the phases ϕ_2, ϕ_3, ϕ_5 and ϕ_{rec}

All spectra were recorded at 298 K with a 600 MHz Bruker NMR spectrometer equipped with a triple resonance cryoprobe. All spectra were processed and analyzed using the software package NMRPipe and peak heights were determined by parabolic interpolation (Delaglio et al. 1995).

Each subspectrum of the 3D ct-HN(CA)CB and ct-HN (COCA)CB experiments was typically recorded with $70(t_1) \times 36(t_2) \times 256(t_3)$ complex points, $t_{1max} = 35$ ms, $t_{2max} = 25$ ms, $t_{3max} = 63.28$ ms, an interscan delay of 1.0 s and 8 scans per increment resulting in a measurement time of 2 days for a pair of subspectra A and B. The time domain data were multiplied with a square cosine function in the direct dimension and cosine functions in the indirect dimensions and zero-filled to $512 \times 128 \times 2,048$ complex points.

GB3 and human ubiquitin were expressed and purified as described previously (Vögeli et al. 2009; Ulmer et al. 2003). The ^{2}H, ^{13}C, ^{15}N-labeled NMR samples contained

500 μl of 2 mM and 350 μl of 4 mM protein solution in 95% H_2O/5% D_2O and 97% H_2O/3% D_2O, 50 mM potassium phosphate buffer, 50 mM NaCl, and pH 7.0 and 5.8, respectively.

The dipole/dipole CCR rates are obtained as

$$\frac{1}{8\tau_{MQ}}\ln\left(\frac{I_{out}^{ZQ}I_{out}^{ZQ}I_{out}^{DQ}I_{out}^{DQ}}{I_{in}^{ZQ}I_{in}^{ZQ}I_{in}^{DQ}I_{in}^{DQ}}\right) = R_{HN/C\beta C\gamma} + R_{HC\beta/NC\gamma} \quad (1)$$

where the intensities of all outer quadruplet peaks are multiplied and divided by those of all inner peaks. Note that the rates originating from $H^N N/C^\beta C^\gamma$ and $H^N C^\beta/NC^\gamma$ interactions cannot be separated and must be considered simultaneously.

The cross-correlated relaxation rate between the dipolar interactions of $I_1 - S_1$ and $I_2 - S_2$ in an anisotropically tumbling rigid molecule is:
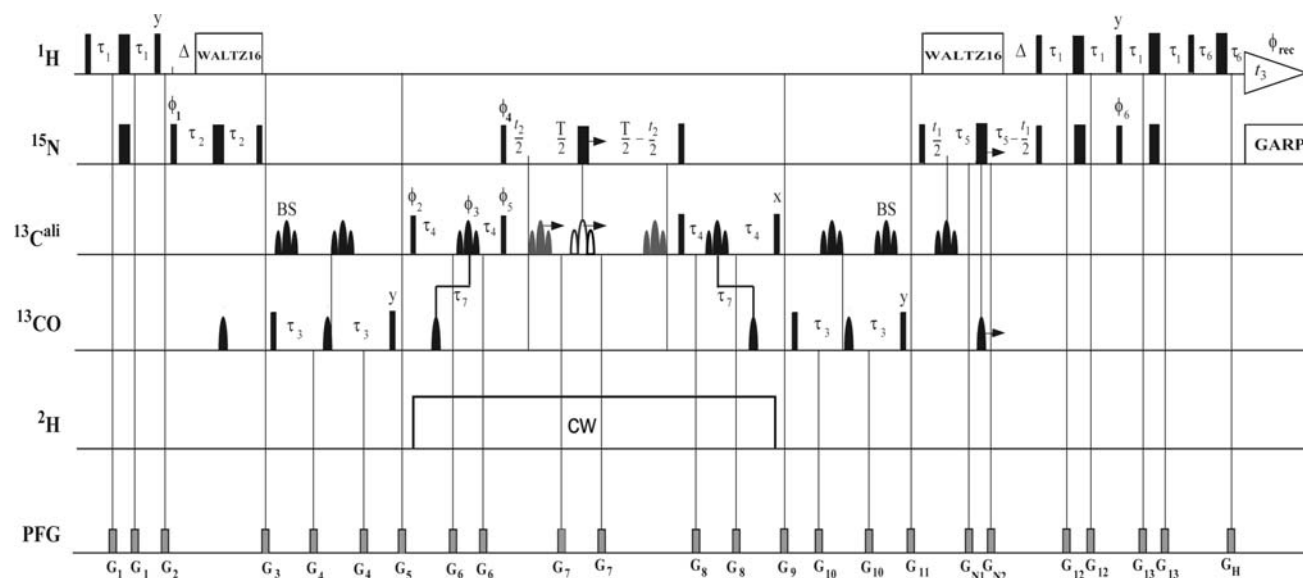
Fig. 2 Pulse sequence of the 3D ct-HN(COCA)CB experiment for measurements of $R = R_{H(i+1)N(i+1)C\beta(i)C\gamma(i)} + R_{H(i+1)C\beta(i)/N(i+1)C\gamma(i)}$ in [ASP, ASN, HIS, PHE, TYR, TRP] residues. The radio-frequency pulses on ^1H, ^{15}N, $^{13}C^{ali}$ and $^{13}C'$ are applied at 4.7, 118, 46.7 and 174 ppm, respectively. *Narrow* and *wide bars* indicate non-selective 90° and 180° pulses. At a 600 MHz field, the *single curved* pulse represents a $^{13}C'$-selective 180° sinc pulse of length $p_{C'}^{\pi} = 150$ μs, and the *black*, *grey* and *white triple curved* ^{13}C ReBURP pulses (Geen and Freeman 1991) are $C^{\alpha/\beta}$, C^{α}, or C^{β}-selective with $p_{C\alpha,\beta}^{\pi} = 500$ μs at 46.7 ppm, $p_{C\alpha}^{\pi} = 1,500$ μs at 60.7 ppm and $p_{C\beta}^{\pi} = 1,000$ μs at 30.7 ppm, respectively. *Vertical lines* connect centered pulses. ^1H-decoupling is achieved with WALTZ16 (Shaka et al. 1983) at a field strength γB_1 of 2.1 kHz and ^{15}N-decoupling is achieved with GARP (Shaka et al. 1985) at a field strength γB_1 of 1.25 kHz. The delays have the following values: $\tau_1 = 2.7$ ms, $\tau_2 = 16$ ms, $\tau_3 = 1/(4J_{C\alpha CO}) = 4.6$ ms, $\tau_4 = 1/(4J_{C\alpha C\beta}) = 7.1$ ms, $\tau_5 = 17$ ms, $\tau_6 = 60$ μs, $\tau_7 = 1/(4J_{C\alpha C\beta}) - 1/(4J_{C\alpha CO}) = 2.5$ ms, $\Delta = 1/(2J_{HN}) = 5.4$ ms, and $T = \tau_{MQ} - 4(p_{Cali}^{\pi/2})/\pi$, where $p_{Cali}^{\pi/2}$ is the length of the rectangular $^{13}C^{ali}$ 90° pulse. The effective evolution during $p_{C\beta}^{\pi}$ is ≈ 100 μs and therefore is assumed to be of the same length as p_N^{π}. Unless indicated otherwise, all radio-frequency pulses are applied with phase x. The phase cycle for the (DQ + ZQ) subspectrum is: $\phi_1 = \{x, -x\}$; $\phi_2 = \{-x, -x, x, x\}$; $\phi_3 = \{y, y, y, y, -y, -y, -y, -y\}$; $\phi_4 = \{x, x, x, x, x, x, x, x, -x, -x, -x, -x, -x, -x, -x, -x\}$; $\phi_5 = \{x, x, x, x, -x, -x, -x, -x\}$; $\phi_6 = -y$; $\phi_{rec} = \{x, -x, -x, x, x, -x, -x, x, -x, x, x, -x, -x, x, x, -x\}$. For the (DQ–ZQ) subspectrum ϕ_3, ϕ_4 and ϕ_5 are increased by 90°. Note that this linear combination is different from the one for the ct-HN(CA)CB experiment (Fig. 1). Pulsed field gradients indicated on the *line marked PFG* are applied along the z-axis with duration/strength of: G_1, 1,200 μs/−9 G/cm; G_2, 2,000 μs/21 G/cm; G_3, 1,000 μs/15 G/cm; G_4, 1,000 μs/6 G/cm; G_5, 2,000 μs/35 G/cm; G_6, 1,000 μs/6 G/cm; G_7, 100 μs/24 G/cm; G_8, 1,000 μs/6 G/cm; G_9, 2,000 μs/35 G/cm; G_{10}, 1,000 μs/6 G/cm; G_{11}, 1,000 μs/15 G/cm; G_{N1}, 200 μs/18 G/cm; G_{N2}, 200 μs/−18 G/cm; G_{12}, 1,200 μs/10.8 G/cm; G_{13}, 1,200 μs/18 G/cm; G_H, 40 μs/−18 G/cm. Quadrature detection in the $^{15}N(t_1)$ is achieved by the ECHO-ANTIECHO method (Kay et al. 1992) applied to ϕ_6 and gradients G_{N1} and G_{N2}, and in the MQ$[^{13}C^\beta, ^{15}N](t_2)$ dimension by the States-TPPI method (Marion et al. 1989) applied to the phases ϕ_2, ϕ_3, ϕ_5 and ϕ_{rec}

$$R_{d(I1S1)/d(I2S2)} =$$
$$\left(\frac{\mu_0}{4\pi}\right)^2 \frac{\gamma_{I1}\gamma_{S1}\gamma_{I2}\gamma_{S2}h^2}{10\pi^2} \frac{1}{r_{I1S1}^3 r_{I2S2}^3} J_{d(I1S1)/d(I2S2)}(0) \quad (2)$$

where μ_0 is the permeability of free space, γ_i is the gyromagnetic ratio of nucleus i, r_{ij} is the distance between nuclei i and j, and h denotes Planck's constant. The spectral density function $J_{d(A)/d(B)}(\omega)$ is given by (Vögeli and Yao 2009)

$$J(\omega) = \sum_{k=-2}^{2} C_k \left[\frac{\tau_k}{1 + (\omega\tau_k)^2}\right] \quad (3)$$

where $1/\tau_k$ are the eigenvalues of the anisotropic diffusion operator $\boldsymbol{D}$ (Favro 1960; Korzhnev et al. 2001):

$$1/\tau_2 = 6\left(D + \sqrt{D^2 - D'^2}\right)$$
$$1/\tau_{-2} = D_x + D_y + 4D_z$$

$$1/\tau_1 = 4D_x + D_y + D_z$$
$$1/\tau_{-1} = D_x + 4D_y + D_z$$
$$1/\tau_0 = 6\left(D - \sqrt{D^2 - D'^2}\right) \quad (4.1\text{–}5)$$

and the coefficients C_k contain the dependency on the vectors $I_1 - S_1$ and $I_2 - S_2$ given by the polar angles θ and φ in the molecular frame:

$$C_2 = \frac{3w^2}{4N^2}\sin^2\theta_A \sin^2\theta_B \cos 2\varphi_A \cos 2\varphi_B$$
$$+ \frac{\sqrt{3}\mu w}{4N^2}\left[\sin^2\theta_A \cos 2\varphi_A (3\cos^2\theta_B - 1)\right.$$
$$\left. + \sin^2\theta_B \cos 2\varphi_B (3\cos^2\theta_A - 1)\right]$$
$$+ \frac{\mu^2}{4N^2}(3\cos^2\theta_A - 1)(3\cos^2\theta_B - 1)$$

$$C_{-2} = \frac{3}{4}\sin^2\theta_A \sin^2\theta_B \sin 2\varphi_A \sin 2\varphi_B$$

$$C_1 = \frac{3}{4}\sin 2\theta_A \sin 2\theta_B \sin\varphi_A \sin\varphi_B$$

$$C_{-1} = \frac{3}{4}\sin 2\theta_A \sin 2\theta_B \cos\varphi_A \cos\varphi_B$$

$$C_0 = \frac{3\mu^2}{4N^2}\sin^2\theta_A \sin^2\theta_B \cos 2\varphi_A \cos 2\varphi_B$$

$$- \frac{\sqrt{3}\mu w}{4N^2}\left[\sin^2\theta_A \cos 2\varphi_A (3\cos^2\theta_B - 1)\right.$$

$$\left. + \sin^2\theta_B \cos 2\varphi_B (3\cos^2\theta_A - 1)\right]$$

$$+ \frac{w^2}{4N^2}(3\cos^2\theta_A - 1)(3\cos^2\theta_B - 1) \qquad (5.1\text{–}5)$$

The following abbreviations are used:

$$D' = \sqrt{\frac{D_x D_y + D_x D_z + D_y D_z}{3}}; \quad D = \frac{D_x + D_y + D_z}{3};$$

$$\mu = \sqrt{3}(D_x - D_y); \quad w = 2D_z - D_x - D_y + 2\Delta$$

$$\Delta = 3\sqrt{D^2 - D'^2}; \quad N = 2\sqrt{\Delta w}$$

Note that the first '+' in (5.1-5) erroneously was '−' and '−' in the expression for μ was '+' in the original publication (Vögeli and Yao 2009).

If dynamic effects are included rigid distances are replaced by effective distances (independence of angular and radial motion is thereby assumed) (Case 1999; Yao et al. 2008b) and $J_{d(A)/d(B)}(\omega)$ becomes

$$J(\omega) = \sum_{k=-2}^{2} C_k \left[\frac{S_k'^2 \tau_k}{1 + (\omega\tau_k)^2} + \frac{(1 - S_k'^2)\tau_k^e}{1 + (\omega\tau_k^e)^2}\right] \qquad (6)$$
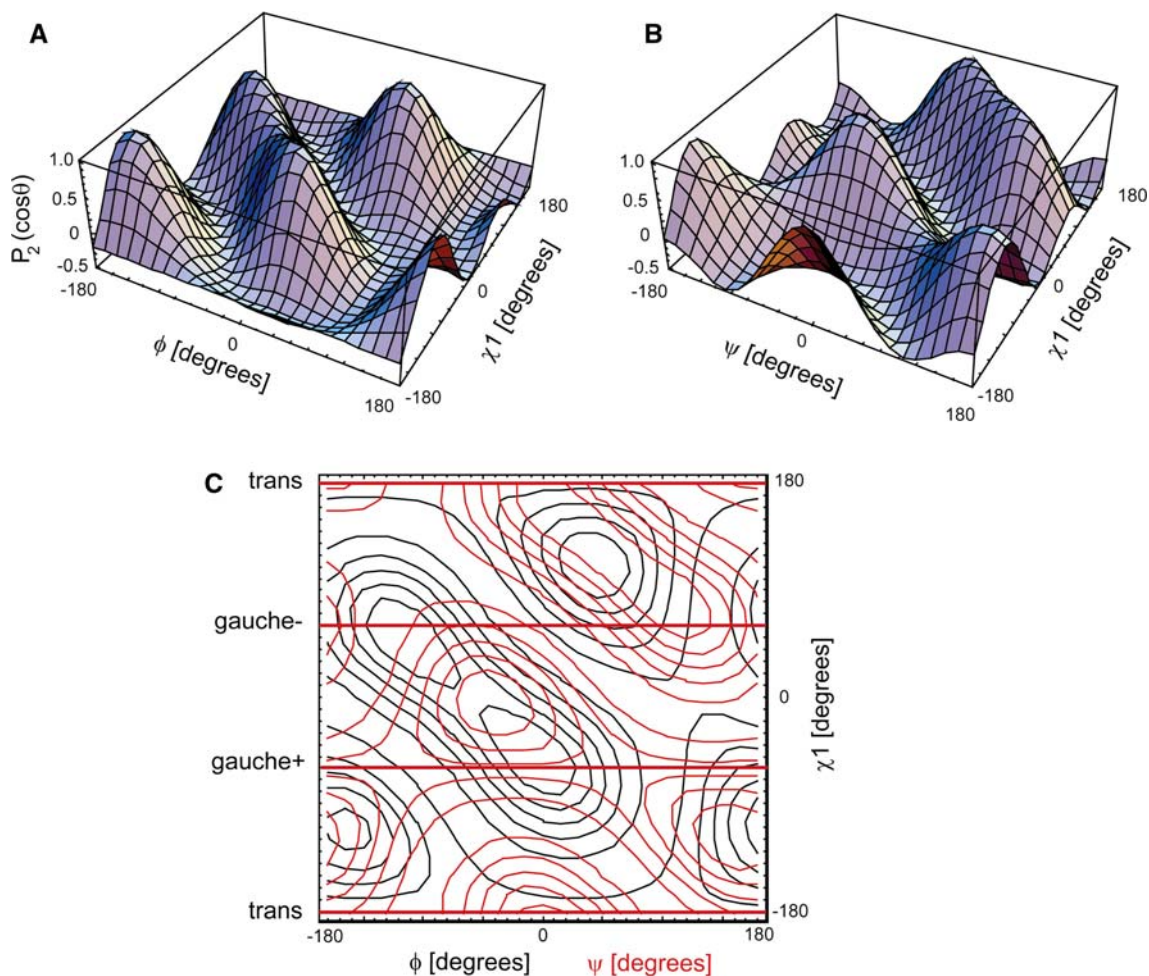
Fig. 3 Simulations of the Legendre polynomial P_2 of the cosine of the projection angle θ as a function of the φ/ψ and $\chi 1$ torsion angles. **a, b** Show 3D plots of P_2 versus $\chi 1$ and φ for the intraresidual rate and ψ for the sequential rate, respectively. In **c**, both P_2 are superimposed in a contour plot. The *red thick lines* represent the idealized staggered side-chain conformations. All other degrees of freedom are frozen, $\omega = 180°$ and the following projection angles are assumed: H^N–N–$C^\alpha = C^\alpha$–CO–N = 116°, CO–N–H^N = 116.5° and N–C^α–C^β = C^α–C^β–C^γ = CO–C^β–C^γ = 109.5°

with

$$\frac{1}{\tau_k^e} \approx \frac{1}{\tau^e} + 2\mathrm{tr}(D) \qquad (7)$$

where 'tr' denotes the matrix trace and

$$S_k'^2 \equiv \frac{\langle C_k \rangle}{C_k} \qquad (8)$$

with the brackets indicating averaging over all conformations.

In case of isotropic molecular tumbling the rate R can be related to the projection angle θ between the two vectors $I_1 - S_1$ and $I_2 - S_2$ as (Daragan and Mayo 1997)

$$R_{I1S1/I2S2} = \left(\frac{\mu_0}{4\pi}\right)^2 \frac{\gamma_H \gamma_N \gamma_C^2 h^2}{10\pi^2} \frac{\tau_c}{r_{I1S1}^3 r_{I2S2}^3} \langle P_2(\cos(\theta)) \rangle. \qquad (9)$$

Figure 3 presents simulations of the Legendre polynomial P_2 of the cosine of the projection angle as a function of the φ/ψ and $\chi1$ torsion angles. Although tumbling anisotropy and fluctuations of the pyramidal and projection angles are neglected the rate sensitivity on small deviations can be appreciated. In particular, the rate has not a symmetric dependence on the angle $\chi1$, as for example in the methods measuring $J_{NC\gamma}$ scalar couplings.

Results

In Fig. 4 ZQ and DQ quadruplets are shown exemplarily for Tyr45 of GB3. Tables 1 and 2 present experimental CCR
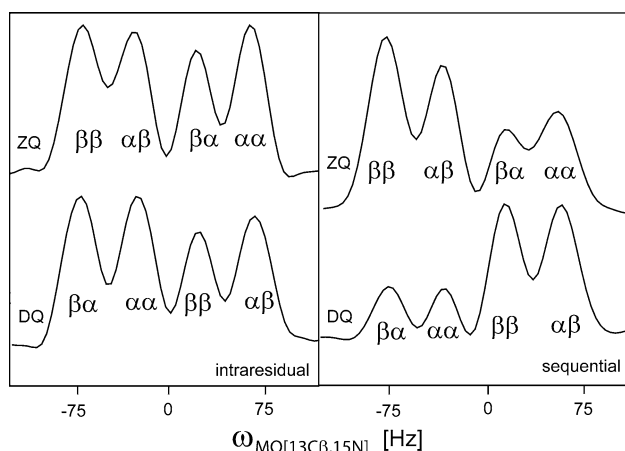
Fig. 4 Traces along the [$^{13}C^\beta$,^{15}N] MQ dimension obtained from the 3D ct-HN(CA)CB experiment (*left panel*) and the ct-HN(COCA)CB experiment (*right panel*). ZQ traces are shown on *top* and DQ traces at the *bottom*. $\gamma\delta$ with γ, $\delta = \alpha$, β are the spin states with respect to C^γ (γ) and H^N (δ), respectively. τ_{MQ} was set to 53 ms for the ct-HN(CA)CB and 59 ms for the ct-HN(COCA)CB. The peaks correspond to the side chain of Tyr45 of GB3. The CCR rates relate C^β–C^γ of Tyr45 to H^N–N of Tyr45 and Asp46, respectively. The *horizontal scale* has an arbitrary offset

rates obtained for GB3 from the experiments ct-HN(CA)CB and ct-HN(COCA)CB, and ubiquitin from the ct-HN(CA)CB, respectively. Individual rate errors are established by repeated measurements with varying τ_{MQ} as indicated in the caption to Fig. 5. From those overall root-mean-square deviations are obtained of 0.27 and 0.18 s^{-1} for the HN(CA)CB and HN(COCA)CB with GB3, respectively, and 0.22 s^{-1} for the HN(CA)CB with ubiquitin. Figure 5 shows experimental CCR rates for GB3 (A) and ubiquitin (B) plotted versus calculated rates based on the NMR structure 2OED with optimized H^N and H$^\alpha$ coordinates (Ulmer et al. 2003; Yao et al. 2008a, b) and the high-resolution X-ray structure 1UBQ (Vijay-Kumar et al. 1987), respectively. Note that the $\chi1$ angles in 2OED are virtually identical to those in the high-resolution 1.1-Å X-ray structure 1IGD (Derrick and Wigley 1994). For GB3 and ubiquitin, a fully anisotropic and an axially symmetric diffusion tensor is assumed, respectively (Hall and Fushman 2003; Tjandra et al. 1995). Although there is an overall qualitative correlation between the experimentally derived and calculated rates, there are outliers which are outside the error range.

In GB3, deviations from the predicted rates are correlated for the intra- and interresidual CCR rates (residues 33, 35, 40, 43 and 52) indicating self consistency of the intra-residual and sequential values. The most extreme outlier is residue 40 which has previously been shown to be extremely flexible around φ (Bouvignies et al. 2005; Vögeli et al. 2007). Interestingly, the RDC H^N-N order parameter of 0.90 does not point to exceptional motion (Yao et al. 2008a, b). However, there appears to be a strong correlated motion present for residues 40 between H^N–N and H$^\alpha$–C$^\alpha$ and therefore C$^\alpha$–C$^\beta$ as well (Vögeli and Yao 2009). It has been shown that for residue 35 $^3J_{H\alpha H\beta2}$ and $^3J_{H\alpha H\beta3}$ are in the intermediate range of 6–8 Hz indicating rotamer averaging and RDCs involving H$^{\beta2}$ and H$^{\beta3}$ do not agree well with 1IGD (Miclet et al. 2005). Clearly, a prediction based on a single conformer representation cannot be compatible with experimental values. The deviation between the calculated and the experimentally measured values of residues 33, 43 and 52 may be attributed to more subtle effects such as a complex interplay between backbone and side-chain dynamics, since the dominant side-chain rotamers in the X-ray structure are in agreement with $^3J_{H\alpha H\beta2}$, $^3J_{H\alpha H\beta3}$ and RDCs involving H$^{\beta2}$ and H$^{\beta3}$ (Miclet et al. 2005) and have been confirmed with $J_{NC\gamma}$ and $J_{COC\gamma}$ measurements (Hu and Bax 1996; Hu et al. 1997) (data not shown) and no evidence for unusually strong backbone flexibility is present (Bouvignies et al. 2005; Yao et al. 2008a, b; Vögeli et al. 2008).

In ubiquitin the rates for residue 39 of −0.17 and 1.27 s^{-1} are not compatible with the X-ray structure (with a $\chi1$ angle of 134.6°) for which the intra- and interresidual rates are calculated to be 0.87 and −0.23 s^{-1}, respectively. A slightly better agreement is obtained if the rates of

Table 1 Experimental and predicted cross-correlated relaxation rates R, φ/ψ and $\chi1$ angles from X-ray structure and NMR ensemble, and RDC order parameters S^{HN} and $S^{H\alpha C\alpha}$ of GB3

Res[a]	R^{exp} [1/s][a]	R^{theo} (X-ray) [1/s][a,b,c]	R^{theo} (NMR) [1/s][a,b,d]	φ/ψ[c,e]	φ/ψ[d,e]	S^{HN} (RDC)[f]	$\chi1$[c]	$\chi1$[d]	$R^{bb,exp}$ [1/s][g]	$R^{bb,theo}$ [1/s][h]	$S^{H\alpha C\alpha}$ (RDC)[f]
Tyr3	0.66	0.42	0.46	−110.7	−114.6 ± 8.9	0.90	−66.5	−64.1 ± 6.3	−11.1	−11.4	0.94
Asp22	−0.40 ± 0.12	−0.40	−0.44	−151.7	−150.6 ± 7.8	0.88	59.8	62.7 ± 12.1	−5.7	−4.9	0.92
Phe30	0.38 ± 0.48	0.47	0.46	−70.7	−67.7 ± 2.1	0.91	−75.8	−75.8 ± 5.6	−3.8	−3.6	
Tyr33	0.74 ± 0.36	0.37	0.29	−58.7	−59.3 ± 2.4	0.91	163.7	175.7 ± 6.4	−0.3	0.2	0.91
Asn35	0.08	0.45	0.42	−61.6	−63.8 ± 8.0	0.87	−73.0	−71.8 ± 14.6	−2.4	−2.1	0.94
Asp36	0.03 ± 0.21	0.22	0.18	−61.2	−61.9 ± 4.4	0.89	−70.4	−72.08 ± 7.7	−1.6	−1.0	0.89
Asn37	0.59 ± 0.29	0.66	0.66	−100.5	−106.4 ± 12.1	0.88	−72.6	−59.0 ± 13.4	−11.0	−10.8	0.90
Asp40	−0.58 ± 0.12	0.43	0.00	−130.0	−142.5 ± 17.8	0.90	177.0	171.0 ± 19.0	−9.6	−11.4	
Trp43	−0.15 ± 0.21	0.54	0.52	−114.3	−106.4 ± 6.6	0.93	−64.0	−65.0 ± 5.7	−9.2	−9.9	0.94
Tyr45	0.69 ± 0.31	0.40	0.39	−139.7	−137.6 ± 11.4	0.92	173.9	172.6 ± 6.1	−11.3	−10.7	0.96
Asp46	0.07	−0.08	0.03	−116.0	−114.2 ± 12.5	0.94	−175.2	−176.4 ± 13.3	−12.0	−11.4	0.91
Phe52	0.42 ± 0.11	0.72	0.61	−103.6	−101.2 ± 5.5	0.95	−69.4	−66.3 ± 8.5	−11.8	−11.5	0.94
Tyr3 s	0.07 ± 0.16	−0.06	−0.04	151.2	−153.5 ± 4.9	0.94	−66.5	−64.1 ± 6.3	−8.2	−8.0	0.94
Phe30 s	0.75 ± 0.01	0.63	0.58	−36.1	−37.4 ± 2.2	0.95	−75.8	−75.8 ± 5.6	−0.9	−1.4	
Tyr33 s	0.20 ± 0.04	−0.38	−0.19	−46.7	−50.4 ± 2.6	0.91	163.7	175.7 ± 6.4	−1.8	−2.2	0.91
Asn35 s*	−0.05 ± 0.03	0.51	0.45	−43.9	−44.3 ± 4.2	0.89	−73.0	−71.8 ± 14.6	−1.4	−1.3	0.94
Asp36 s	0.77 ± 0.07	0.39	0.34	−29.2	−24.8 ± 9.5	0.88	−70.4	−72.08 ± 7.7	−2.0	−1.5	0.89
Asp40 s	−0.06 ± 0.26	0.44	0.12	91.6	−123.5 ± 17.0	0.77	177.0	171.0 ± 19.0	−10.4	−10.5	
Trp43 s	0.06 ± 0.27	−0.23	−0.24	147.3	−138.0 ± 7.2	0.91	−64.0	−65.0 ± 5.7	−8.9	−9.2	0.94
Tyr45 s	0.67 ± 0.34	0.60	0.64	130.3	−131.9 ± 11.0	0.94	173.9	172.6 ± 6.1	−7.6	−6.1	0.96
Asp46 s	0.57 ± 0.12	0.49	0.41	109.3	−107.3 ± 10.0	0.87	−175.2	−176.4 ± 13.3	−11.0	−9.6	0.91
Phe52 s	0.26 ± 0.13	0.06	−0.07	146.3	138.8 ± 10.4	0.95	−69.4	−66.3 ± 8.5	−10.7	−10.7	0.94

[a] Cross-correlated relaxation rate for res i between intraresidual $H^N(i)N(i)C^\beta(i)C^\gamma(i)$ and $H^N(i)N(i)C^\beta(i)N(i)C^{\gamma'}(i)$

[b] The anisotropic tumbling tensor has been used as presented in (Hall and Fushman 2003)

[c] Obtained from pdb code 2OED

[d] Obtained from a 160 conformers ensemble derived from RDCs, ^{15}N relaxation order parameters and crystallographic temperature factors (Clore and Schwieters 2006)

[e] φ For intraresidual and ψ for interresidual rates

[f] Obtained from reference (Yao et al. 2008a, b)

[g] R^{bb} are the summed experimental backbone cross-correlated relaxation rates $R_{d(HN)/d(H\alpha C\alpha)} + R_{d(H\alpha N)/d(HC\alpha)}$ as obtained in reference (Vögeli and Yao 2009)

[h] R^{bb} are the summed predicted backbone cross-correlated relaxation rates $R_{d(HN)/d(H\alpha C\alpha)} + R_{d(H\alpha N)/d(HC\alpha)}$ based on uncorrelated motion of RDC-derived H^N–N and H^α–C^α order parameters as obtained in reference (Yao et al. 2008a, b)

Table 2 Experimental and predicted cross-correlated relaxation rates R, φ/ψ and $\chi 1$ angles from X-ray and NMR structures, and J couplings of ubiquitin

Res[a]	R^{exp} [1/s][a]	R^{theo} (X-ray) [1/s][a,b,c]	R^{theo} (NMR) [1/s][a,b,d,e]	R^{theo} (NMR) [1/s][a,b,e,f]	φ/ψ[g] (X-ray)[c]	φ/ψ[g] (NMR)[d]	φ/ψ[g] (NMR)[f]	$\chi 1$ (X-ray)[c]	$\chi 1$ (NMR)[d]	$\chi 1$ (NMR)[f]	$^3J_{NC\gamma}$ [Hz]	$^3J_{C'C\gamma}$ [Hz]
Asp21	0.69 ± 0.24	0.69	0.68	0.49	−71.0	−70.5	−72.8 ± 11.0	−80.6	−77.8 ± 0.5	−95.1 ± 32.8		5.5[i]
Asn25	0.33 ± 0.50	0.21	0.34	0.40	−65.5	−66.2	−71.4 ± 10.7	177.5	−135.4 ± 51.8	−137.6 ± 43.7		3.4[i]
Asp32	0.45 ± 0.15	0.37	0.28	0.54	−53.4	−60.4	−60.2 ± 13.3	−150.1	−139.8 ± 56.3	−178.9 ± 13.1		3.3[i]
Asp39	−0.17 ± 0.13	0.87	0.24	0.31	−68.2	−72.0	−64.8 ± 15.9	134.6	−27.6 ± 86.9	−170.6 ± 64.5		1.8[i]
Phe45	0.60 ± 0.19	0.34	0.43	0.27	−144.3	−139.3	−137.9 ± 19.2	178.0	−175.5 ± 2.1	177.2 ± 26.6	2.1[h]	0.4[h]
Asp52	0.01 ± 0.05	0.30	0.60	0.06	−48.2	−68.8	−63.4 ± 32.8	−78.0	−68.8 ± 1.2	−77.2 ± 68.3		
Asp58	0.42 ± 0.11	0.28	0.39	0.33	−55.6	−62.1	−68.3 ± 10.8	−73.0	−69.7 ± 1.3	−83.4 ± 41.0		5.6[i]
Asn60	0.25 ± 0.16	0.75	−0.44	0.28	57.9	50.1	69.0 ± 24.7	−159.1	−59.2 ± 73.8	−123.1 ± 83.9		2.0[h]
Asp32 s	−0.40 ± 0.25	−0.71	−0.32	−0.30	36	1.69	−39.3 ± 11.7	−150.1	−139.8 ± 56.3	−178.9 ± 13.1		3.3[i]
Asp39 s	1.27 ± 0.24	−0.23	0.41	−0.33	39	1.62	−23.3 ± 25.7	134.6	−27.6 ± 86.9	−170.6 ± 64.5		1.8[i]
Gly10	1.14 ± 0.17	0.47	0.73	0.67	77.4	94.6	114.6 ± 26.7					
Gly35	0.56	0.57	0.59	0.34	81.2	82.46	95.5 ± 24.2					
Gly47	0.85 ± 0.04	−0.06	0.51	0.46	61.7	82.0	107.4 ± 51.8					
Gly75	−0.23	0.67	0.51	0.68		89.9	−169.4 ± 61.5					

[a] Cross-correlated relaxation rate for res i between intraresidual $H^N(i)N(i)/C^\beta(i)C^\gamma(i)$ and $H^N(i)C^\beta(i)/N(i)C^\gamma(i)$; for res is between sequential $H^N(i+1)N(i+1)/C^\beta(i)C^\gamma(i)/N(i+1)C^\gamma(i)$ and $H^N(i+1)C^\beta(i)C^\gamma(i)$ and $H^N(i+1)C^\beta(i)/N(i+1)C^\gamma(i)$; and for glycines res i between $H^N(i)N(i)/C^\alpha(i)CO(i)$ and $H^N(i)C^\alpha(i)/N(i)CO(i)$

[b] The symmetric tumbling tensor has been used as presented in (Tjandra et al. 1995)

[c] X-ray structure with pbd code 1UBQ (Vijay-Kumar et al. 1987)

[d] NMR structure with pbd code 1D3Z (Cornilescu et al. 1998)

[e] CCR rates are averaged over ensemble

[f] NMR structure with pbd code 2k39 (Lange et al. 2008)

[g] φ For intraresidual and ψ for interresidual rates

[h] Obtained from reference (Hu et al. 1997)

[i] Obtained from reference (Hu and Bax 1996)
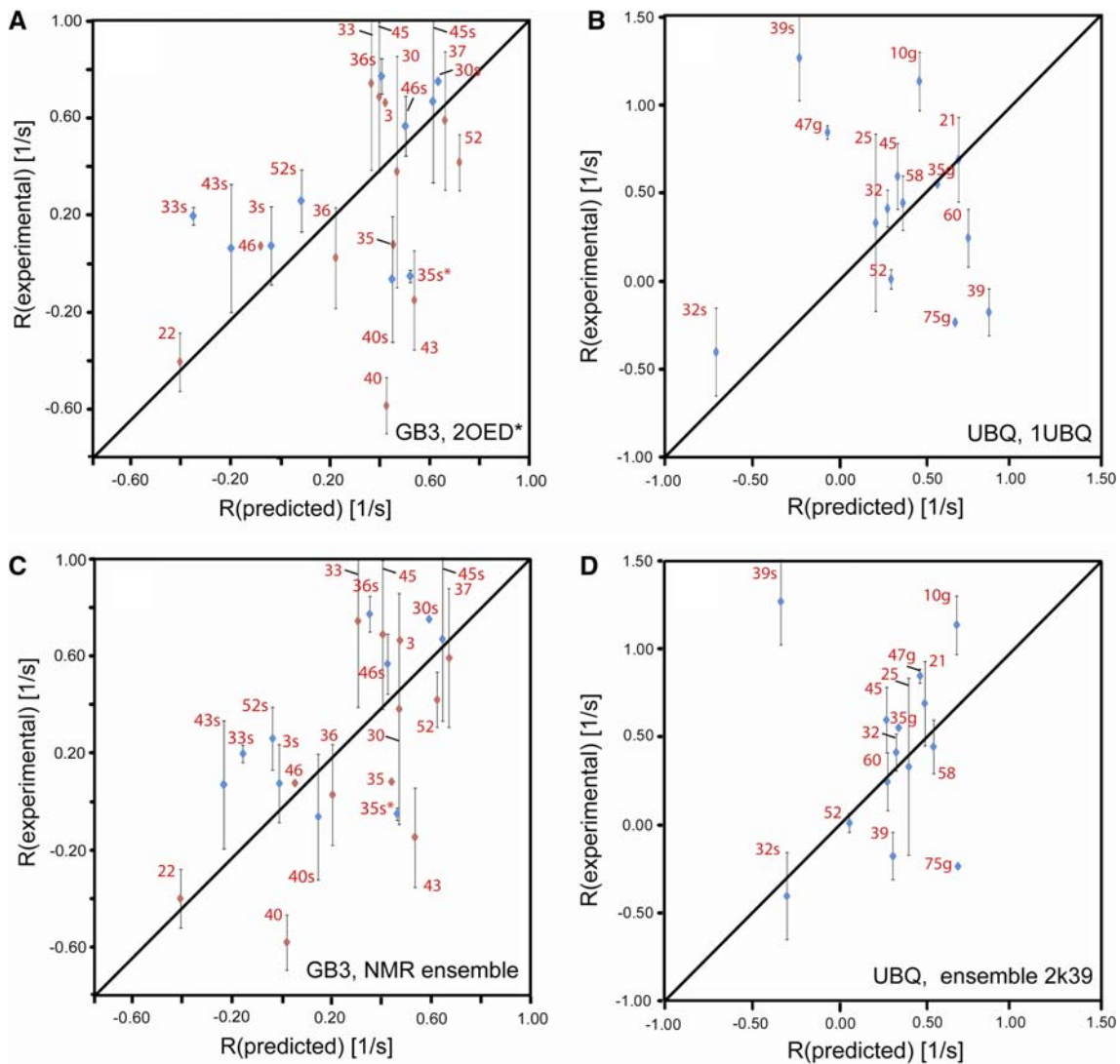
Fig. 5 Experimental versus calculated cross-correlated relaxation rates $R = R_{HN/C\beta C\gamma} + R_{HC\beta/NC\gamma}$ where sequential rates are marked with *s*, rates obtained with low S/N with '*', and rates of glycine $R = R_{HN/C\alpha CO} + R_{HC\alpha/NCO}$ with *g*. Fully anisotropic and symmetric molecular tumbling is assumed for GB3 and ubiquitin, respectively (Hall and Fushman 2003; Tjandra et al. 1995). All spherical fluctuations are eliminated by setting the bond lengths of H^N–N to 1.02 Å and C^β–C^γ to 1.53 Å. Rates of GB3 predicted from pdb code 2OED with optimized H^N and H^a coordinates (Yao et al. 2008a, b) are shown in **a**, and from a 160 conformer ensemble (Clore and Schwieters 2006) in **c**. Rates of ubiquitin predicted from the structure deposited under pdb code 1UBQ (Vijay-Kumar et al. 1987) are shown in **b**, and from a 116 conformer ensemble (pdb code 2k39, Lange et al. 2008) in **d**. *Random errors* are calculated from measurements with τ_{MQ} set to 43, 53 and 63 ms (HN(CA)CB), and 53 and 59 ms (HN(COCA)CB) for GB3, and 48 and 54 ms (HN(CA)CB) for ubiquitin, respectively

interest are calculated from the NMR structure 1D3Z (0.24 and 0.41 s^{-1}). This structure is a 10 conformer ensemble which is tightly constrained in the backbone (the dihedral angle rmsd is typically 1°). The rate of residue 60 of ubiquitin is neither compatible with the X-ray (−159.1°) nor with the NMR structure (−59.2°). Since in these two structures the χ_1 angle differs by 100° an averaging between these two populations may actually be present. Other mismatches are the glycines 47 and 75 attributed to the typically larger fluctuations of φ of glycines than of other amino acid residues as exemplified by the more than 20° difference between the X-ray and the NMR structure

for Gly47. Furthermore, Gly75 is located at the C terminus and hence high flexibility is expected.

In the recent years, the focus of NMR structure calculation has shifted from single conformer to ensemble representations (Clore and Schwieters 2004a, b; Lindorff-Larsen et al. 2005). For both proteins under consideration in this study, ensembles have been calculated satisfying the following constraints: ^{15}N relaxation data, backbone RDCs, crystallographic B-factors and across-hydrogen J couplings for GB3 (Clore and Schwieters 2004a, b, 2006; Markwick et al. 2007); similarly, for ubiquitin ^{15}N relaxation data, backbone RDCs, NOEs, across-hydrogen

J couplings, and *J* couplings defining backbone dihedral angles and χ1 (Clore and Schwieters 2004a, b; Lindorff-Larsen et al. 2005; Lange et al. 2008). In this study, CCR rate predictions are achieved by rotating individually every ensemble conformer into the according diffusion tensor frame. Figure 5b, d show plots of the experimental rates versus rates predicted from the 160 conformer GB3 ensemble as presented in (Clore and Schwieters 2006) and the 116 conformer ubiquitin ensemble 2k39 (Lange et al. 2008). For GB3 the outliers are the same as for the single structure representation. The only significant rate change is obtained for residue 40. This change is a cumulative effect of 12° and 6° differences in the φ and χ1 angles and unusually large fluctuations of those. However, the experimental rate is still 0.58 s^{-1} smaller. Otherwise the φ angles are similar and all side chains are in the same rotamer state as in the single structure representation. Notably, in residue 35 the averaged χ1 angle deviates only by 1.2° from 2OED and has a small rmsd of 14.6°. Such values are clearly neither compatible with the CCR data nor with $^3J_{H\alpha H\beta 2}$, $^3J_{H\alpha H\beta 3}$ and RDCs involving H$^{\beta 2}$ and H$^{\beta 3}$ (Miclet et al. 2005). Since the ensemble has been calculated with minimal angular fluctuations that satisfy experimental parameters, it is not surprising that the predicted rates do not agree better with the experimental values than those from 2OED. In contrast, for ubiquitin the overall agreement between experimental CCR rates and those calculated from the NMR ensemble 2k39 is improved when compared to the single structure representation 1UBQ (Fig. 5d). For example, the rate calculated for residue 60 is almost the same as the experimental one (0.25 and 0.28 s^{-1}), lying between the two extremes obtained from the 1UBQ and 1D3Z structures. For glycine 47, the deviations to the experimental values are also significantly reduced when compared with the single structure representation. Only the rates of the most extreme outlier, residue 39, as well as of Gly75 and Gly10 do not agree appreciably better. Interestingly, both the experimental intra- and interresidual rates of residue 39 agree best with those predicted from 1D3Z.

Discussion and conclusion

The presented CCR measurements between both intraresidual and sequential H^N–N and C$^\beta$–C$^\gamma$ dipolar couplings in Asp, Asn and the aromatic amino acid residues enables cross validation of the rotamer states of χ1 provided that the backbone dihedral angles are known. The larger experimental error obtained than for the CCR rates between backbone H$^\alpha$–C$^\alpha$ and H^N–N can thereby be tolerated because the effect of side-chain population averaging is expected to cause larger changes in the rates (Vögeli

and Yao 2009). Due to the long time that the magnetization resides in the transverse plane the applicability of the pulse sequences with the τ$_{MQ}$ listed in the figure captions 1 and 2 are restricted to small proteins since signal losses during the transfer elements and nitrogen evolution increase with increasing tumbling time. However, since both the auto- and the cross-correlated relaxation during τ$_{MQ}$ are approximately proportional to the tumbling time proteins of any size undergo the same signal loss using an optimal τ$_{MQ}$, which must be adjusted for larger proteins. In other words, a larger protein has larger CCR rates and needs concomitantly less time to redistribute intensities in a quadruplet. Therefore, τ$_{MQ}$ must be chosen shorter for an optimal signal-to-noise ratio. There may arise however the following problem. Because in constant time evolution periods the line widths of the peaks do not depend on the protein size but on the maximal time increment, for large proteins τ$_{MQ}$ may have to be set such that the quadruplet cannot be sufficiently resolved. In such cases alternative pulse sequences can be set up following the concept that the quadruplets of the ZQ and DQ spectra can be separated into four spectra (two ZQ and two DQ) each containing only a doublet split by $J_{C\beta C\gamma}$ corresponding either to spin state α or β with respect to H^N (Vögeli and Pervushin 2002). An additional gain of a factor $\sqrt{2}$ in sensitivity has been demonstrated by mixing ZQ and DQ coherences (Yang and Kay 1998). However, this approach requires six 180° pulses on the four spins involved. In that case, at least one pulse is applied on the passively coupled spin and selective pulses are involved which further complicate a reliable extraction of the rates.

The presented CCR measurements between both intra-residual and sequential H^N–N and C$^\beta$–C$^\gamma$ dipolar couplings in Asp, Asn and the aromatic amino acid residues revealed considerable deviation from CCR rates predicted from single structure representations. This observation agrees with studies of ^{13}C relaxation data (Houben and Boelens 2004; LeMaster and Kushlan 1996) and ^{2}H relaxation, *J* coupling and RDC data from side chains with methyl groups (Mittermaier et al. 1999; Chou et al. 2003; Farès et al. 2009). Furthermore, CCR rates calculated from an ubiquitin ensemble significantly improved the agreement with the experimental values. However, the CCR rates calculated from an ensemble representation of GB3 are not in better agreement than those extracted from a highly accurate single structure representation. Generally, it appears that if any *J* couplings defining χ1 at all have been used as an input for ensemble structure calculations they were almost exclusively restricted to methyl-group bearing side chains. In this respect, it is hardly surprising that CCR rates predicted from ensembles do not in all cases agree better with those obtained from single NMR and X-ray representations. It should be pointed out again that the

CCR rates depend rather sensitively on both dihedral angles and fluctuations thereof (see Fig. 3). These findings highlight the need for new NMR input data considering the side chain for structure and ensemble calculation.

In a future application, such CCR measurements may be used to study side-chain dynamics on all timescales (Pelupessy et al. 2003; Vugmeyster et al. 2004). An interesting prospect is an analysis of correlated fluctuations of the φ/ψ and $\chi 1$ angles. For example, such main chain-side chain "crankshaft" motions have been used to interpret Lipari-Szabo order parameters of side-chain carbons of *Escherichia coli* thioredoxin (LeMaster and Kushlan 1996). Once the individual fluctuations of these angles are precisely known on the relevant timescale (as obtained from RDCs or scalar couplings) the compatibility of combined fluctuation models can be checked against the CCR data. Alternatively, RDC order parameters of H^N–N and C^β–C^γ can be used (Yao et al. 2008a, b). In this respect, we are currently developing experiments providing more dipole–dipole projections and more NMR probes based on quantitative ^1H–^1H NOEs (Vögeli et al. 2009) and ^{13}C–^{13}C-NOEs (Houben and Boelens 2004). These probes are required to provide a more detailed picture of side-chain motion and possible correlation with backbone fluctuations.

References

Bouvignies G, Bernado P, Meier S, Cho K, Grzesiek S, Brüschweiler R, Blackledge M (2005) Identification of slow correlated motions in proteins using residual dipolar and hydrogen-bond scalar couplings. Proc Natl Acad Sci USA 102:13885–13890

Brüschweiler R, Griesinger C, Ernst RR (1989) Correlated motion monitored by nmr relaxation in the rotating frame. A source of structural and dynamic information on macromolecules. J Am Chem Soc 111:8034–8035

Brüschweiler R, Roux B, Blackledge M, Griesinger C, Karplus M, Ernst RR (1992) Influence of rapid intramolecular motion on NMR cross-relaxation rates. A molecular dynamics study of antamanide in solution. J Am Chem Soc 114:2289–2302

Brutscher B, Skrynnikov NR, Bremi T, Brüschweiler R, Ernst RR (1998) Quantitative investigation of dipole-CSA cross-correlated relaxation by ZQ/DQ Spectroscopy. J Magn Reson 130:346–351

Carlomagno T, Bermel W, Griesinger C (2003) Measuring the χ_1 torsion angle in protein by CH-CH cross-correlated relaxation: a new resolution-optimised experiment. J Biomol NMR 27:151–157

Case DA (1999) Calculation of nmr dipolar coupling strengths in modelpeptides. J Biomol NMR 15:95–102

Cavanagh J, Fairbrother WJ, Palmer AG, Rance M, Skleton NJ (2007) Protein NMR spectroscopy, principles and pratice. Academic Press, San Diego

Chiarparin E, Pelupessy P, Ghose R, Bodenhausen G (1999) Relaxation of two-spin coherence due to cross-correlated fluctuations of dipole-dipole couplings and anisotropic shifts in nmr of 15 N, 13C-labeled biomolecules. J Am Chem Soc 121:6876–6883

Chou JJ, Case DA, Bax A (2003) Insights into the mobility of methyl-bearing side chains in proteins from $^3J_{CC}$ and $^3J_{CN}$ couplings. J Am Chem Soc 125:8959–8966

Clore GM, Schwieters CD (2004a) Amplitudes of protein backbone dynamics and correlated motions in a small α/β protein: correspondence of dipolar coupling and heteronuclear relaxation measurements. Biochemistry 43:10678–10691

Clore GM, Schwieters CD (2004b) How much backbone motion in ubiquitin is required to account for dipolar coupling data measured in multiple alignment media as assessed by independent cross-validation? J Am Chem Soc 126:2923–2938

Clore GM, Schwieters CD (2006) Concordance of residual dipolar couplings, backbone order parameters and crystallographic B-factors for a small alpha/beta protein: a unified picture of high probability, fast atomic motions in proteins. J Mol Biol 355:879–886

Cornilescu G, Marquardt JL, Ottiger M, Bax A (1998) Validation of protein structure from anisotropic carbonyl chemical shifts in a dilute liquid crystalline phase. J Am Chem Soc 120:6836–6837

Dalvit C, Bodenhausen G (1988) Evidence for dipolar cross-correlation from triple-quantum-filtered two-dimensional exchange nmr spectroscopy. J Am Chem Soc 110:7924–7926

Daragan VA, Mayo KH (1997) Motional model analyses of protein and peptide dynamics using ^{13}C and ^{15}N nmr relaxation. Prog Nucl Magn Reson Spectrosc 31:63–105

Delaglio F, Grzesiek S, Vuister GW, Zhu G, Pfeifer J, Bax A (1995) nmrPipe—a multidimensional spectral processing system based on unix pipes. J Biomol NMR 6:277–293

Derrick JP, Wigley DB (1994) The 3rd Igg-binding domain from streptococcal protein-G—an analysis by X-ray crystallography of the structure alone and in a complex with fab. J Am Chem Soc 243:906–918

Ernst M, Ernst RR (1994) Heteronuclear dipolar cross-correlated cross relaxation for the investigation of side-chain motions. J Magn Reson A 110:202–213

Farès C, Lakomek NA, Walter KFA, Frank BTC, Meiler J, Becker S, Griesinger C (2009) Accessing ns-µs side-chain dynamics in ubiquitin with methyl RDCs. J Biomol NMR 45:23–44

Favro LD (1960) Theory of the rotational brownian motion of a free rigid body. Phys Rev 119:53–62

Geen H, Freeman R (1991) Band-selective radiofrequency pulses. J Magn Reson 93:93–141

Goldman M (1984) Interference effects in the relaxation of a pair of unlike spin-1/2 nuclei. J Magn Reson 60:437–452

Hall JB, Fushman D (2003) Characterization of the overall and local dynamics of a protein with intermediate rotational anisotropy: Differentiating between conformational exchange and anisotropic diffusion in the B3 domain of protein G. J Biomol NMR 27:261–275

Houben K, Boelens R (2004) Side chain dynamics monitored by 13C–13C cross-relaxation. J Biomol NMR 29:151–166

Hu JS, Bax A (1996) Measurement of three-bond 13C–13C J couplings between carbonyl and carbonyl/carboxyl carbons in isotopically enriched proteins. J Am Chem Soc 118:8170–8171

Hu JS, Grzesiek S, Bax A (1997) Two-dimensional NMR methods for determining χ_1 angles of aromatic residues in proteins from three-bond $J_{C'C\gamma}$ and $J_{NC\gamma}$ couplings. J Am Chem Soc 119:1803–1804

Hu H, Hermans J, Lee AL (2005) Relating side-chain mobility in proteins to rotameric transitions: insights from molecular dynamics simulations and NMR. J Biomol NMR 32:151–162

Kay LE, Torchia DA, Bax A (1989) Backbone dynamics of proteins as studied by ^{15}N inverse detected heteronuclear NMR spectroscopy: application to staphylococcal nuclease. Biochemistry 28:8972–8979

Kay LE, Keifer P, Saarinen T (1992) Pure absorption gradient enhanced heteronuclear single quantum correlation spectroscopy with improved sensitivity. J Am Chem Soc 114:10663–10665

Korzhnev DM, Billeter M, Arseniev AS, Orekhov VY (2001) Nmr studies of brownian tumbling and internal motions in proteins. Prog Nucl Magn Reson Spectrosc 38:197–266

Lakomek NA, Walter KFA, Farès C, Lange OF, de Groot BL, Grubmüller H, Brüschweiler R, Munk A, Becker S, Meiler J, Griesinger C (2008) Self-consistent residual dipolar coupling based model-free analysis for the robust determination of nansecond to microsecond protein dynamics. J Biomol NMR 41:139–155

Lange OF, Lakomek NA, Farès C, Schröder GF, Walter KFA, Becker S, Meiler J, Grubmüller H, Griesinger C, de Groot BL (2008) Recognition dynamics up to microseconds revealed from an RDC-derived ubiquitin ensemble in solution. Science 320: 1471–1475

LeMaster DM, Kushlan DM (1996) Dynamical mapping of e.coli thioredoxin via ^{13}C NMR relaxation analysis. J Am Chem Soc 118:9255–9264

Lindorff-Larsen K, Best RB, DePristo MA, Dobson CM, Vendruscolo M (2005) Simultaneous determination of protein structure and dynamics. Nature 433:128–132

Lipari G, Szabo A (1982) Model-free approach to the interpretation of nuclear magnetic resonance relaxation in macromolecules 1. Theory and range of validity. J Am Chem Soc 104:4546–4559

Marion D, Ikura M, Tschudin R, Bax A (1989) Rapid recording of 2D nmr spectra without phase cycling. Application to study of hydrogen exchange in proteins. J Magn Reson 85:393–399

Markwick PRL, Bouvignies G, Blackledge M (2007) Exploring multiple timescale motions in protein GB3 using accelerated molecular dynamics and nmr spectroscopy. J Am Chem Soc 129:4724–4730

Markwick PRL, Showalter SA, Bouvignies G, Brüschweiler R, Blackledge M (2009) Structural dynamics of protein backbone φ angles: extended molecular dynamics simulations versus experimental ^{3}J scalar couplings. J Biomol NMR 45:17–21

Meiler J, Pompers JJ, Peti W, Griesinger C, Brüschweiler R (2001) Model-free approach to the dynamic interpretation of residual dipolar couplings in globular proteins. J Am Chem Soc 123:6098–6107

Miclet E, Boisbouvier J, Bax A (2005) Measurement of eight scalar and dipolar couplings for methane-methylene pairs in proteins and nucleic acids. J Biomol NMR 31:201–216

Mittermaier A, Kay LE (2006) New tools provide new insights in NMR studies of protein dynamics. Science 312:224–228

Mittermaier A, Kay LE, Forman-Kay JD (1999) Analysis of deuterium relaxation-derived methyl axis order parameters and correlation with local structure. J Biomol NMR 13:181–185

Muhandrin DR, Yamazaki T, Sykes BD, Kay LE (1995) Measurement of ^{2}H T_1 and $T_{1\rho}$ relaxation times in uniformly ^{13}C-labeled and fractionally ^{2}H-labeled proteins in solution. J Am Chem Soc 117:11536–11544

Nirmala NR, Wagner G (1989) Measurement of 13C spin-spin relaxation times by two-dimensional heteronuclear 1H–13C correlation spectroscopy. J Magn Reson 82:659–661

Pelupessy P, Chiarparin E, Ghose R, Bodenhausen G (1999) Efficient determination of angles subtended by C^α-H^α and N-H^N vectors in proteins via dipole–dipole cross-correlation. J Biomol NMR 13:375–380

Pelupessy P, Ravindranathan S, Bodenhausen G (2003) Correlated motions of successive amide N-H bonds in proteins. J Biomol NMR 25:265–280

Perez C, Löhr F, Rüterjans H, Schmidt JM (2001) Self-consistent karplus parametrization of ^{3}J couplings depending on the polypeptide sidechain torsion χ_1. J Am Chem Soc 123:7081–7093

Peti W, Meiler J, Brüschweiler R, Griesinger C (2002) Model-free analysis of protein backbone motion from residual dipolar couplings. J Am Chem Soc 124:5822–5833

Reif B, Hennig M, Griesinger C (1997) Direct measurement of angles between bond vectors in high-resolution NMR. Science 276:1230–1233

Salmon L, Bouvignies G, Markwick P, Lakomek N, Showalter S, Li DW, Walter K, Griesinger C, Brüschweiler R, Blackledge M (2009) Protein conformational flexibility from structure-free analysis of NMR dipolar couplings: quantitative and absolute determination of backbone motion in ubiquitin. Angew Chem Int Ed Engl 48:4154–4157

Schmidt JM (2007) A versatile component-coupling model to account for substituent effects: application to polypeptide φ and χ_1 torsion related ^{3}J data. J Magn Reson 186:34–50

Shaka AJ, Keeler J, Frenkiel T, Freeman R (1983) An improved sequence for broadband decoupling: WALTZ-16. J Magn Reson 52:335–338

Shaka AJ, Barker PB, Freeman R (1985) Computer-optimized decoupling scheme for wideband application and low-level operation. J Magn Reson 64:547–552

Tjandra N, Bax A (1997) Direct measurement of distances and angles in biomolecules by NMR in a dilute liquid crystalline medium. Science 278:1111–1114

Tjandra N, Feller SE, Pastor RW, Bax A (1995) Rotational diffusion anisotropy of human ubiquitin from 15 N NMR relaxation. J Am Chem Soc 117:12562–12566

Tolman JR (2002) A novel approach to the retrieval of structural and dynamic information from residual dipolar couplings using several oriented media in biomolecular NMR spectroscopy. J Am Chem Soc 124:12020–12030

Ulmer TS, Ramirez BE, Delaglio F, Bax A (2003) Evaluation of backbone proton positions and dynamics in a small protein by liquid crystal NMR spectroscopy. J Am Chem Soc 125:9179–9191

Vijay-Kumar S, Bugg CE, Cook WJ (1987) Structure of ubiquitin refined at 1.8 A resolution. J Mol Biol 194:531–544

Vögeli B, Pervushin K (2002) Trosy experiment for refinement of backbone ψ and ϕ by simultaneous measurements of cross-correlated relaxation rates and 3, 4JHaHN coupling constants. J Biomol NMR 24:291–300

Vögeli B, Yao L (2009) Correlated dynamics between HN and HC bonds observed by NMR cross relaxation. J Am Chem Soc 131:3668–3678

Vögeli B, Kovacs H, Pervushin K (2004) Measurements of side-chain 13C–13C residual dipolar couplings in uniformly deuterated proteins. J Am Chem Soc 126:2414–2420

Vögeli B, Ying JF, Grishaev A, Bax A (2007) Limits on variations in protein backbone dynamics from precise measurements of scalar couplings. J Am Chem Soc 129:9377–9385

Vögeli B, Yao L, Bax A (2008) Protein backbone motions viewed by intraresidue and sequential H^N–H^α residual dipolar couplings. J Biomol NMR 41:17–28

Vögeli B, Segawa TF, Leitz D, Sobol A, Choutko A, Trzesniak D, van Gunsteren W, Riek R (2009) Exact distances and internal dynamics of perdeuterated ubiquitin from NOE buildups. J Am Chem Soc (in press)

Vugmeyster L, Pelupessy P, Vugmeister BE, Abergel D, Bodenhausen G (2004) Cross-correlated relaxation in nmr of macromolecules in the presence of fast and slow internal dynamics. C R Physique 5:377–386

Wüthrich K (1986) NMR of proteins and nucleic acid. Wiley, New York

Xu J, Xue Y, Skrynnikov NR (2009) Detection of nanosecond time scale side-chain jumps in a protein dissolved in water/glycerol solvent. J Biomol NMR 45:57–72

Yang DW, Kay LE (1998) Determination of the protein backbone dihedral angle ψ from a combination of nmr-derived cross-correlation spin relaxation rates. J Am Chem Soc 120: 9880–9887

Yang DW, Mittermaier A, Mok YK, Kay LE (1998) A study of protein side-chain dynamics from new 2H auto-correlation and 13C cross-correlation NMR experiments: application to the N-terminal SH3 domain from drx. J Mol Biol 276:939–954

Yao L, Vögeli B, Torchia DA, Bax A (2008a) Simultaneous NMR study of protein structure and dynamics using conservative mutagenesis. J Phys Chem B 112:6045–6056

Yao L, Vögeli B, Ying JF, Bax A (2008b) Nmr determination of amide N-H equilibrium bond length from concerted dipolar coupling measurements. J Am Chem Soc 130:16518–16520

Zheng Y, Yang D (2004) Measurement of dipolar cross-correlation in methylene groups in uniformly ^{13}C-, ^{15}N-labeled proteins. J Biomol NMR 28:103–116